New capabilities in high-resolution neutron Larmor diffraction at ORNL

Authors

Fankang Li[1], Hao Feng[2], Alexander N. Thaler[1], Steven R. Parnell[3], Lowell Crow[1], Masaaki Matsuda[1], Feng Ye[1], Tsuyoshi Kimura[4], Jaime A. Fernandez-Baca[1] and Roger Pynn[1,2]

[1] Neutron Sciences Directorate, Oak Ridge National Laboratory, Oak Ridge, TN, 37830, USA

[2] Center for Exploration of Energy and Matter, Indiana University, Bloomington, IN, 47408, USA

[3] Faculty of Applied Sciences, Delft University of Technology, Mekelweg 15, Delft, 2629 JB, The Netherlands

[4] Department of Advanced Materials Science, The University of Tokyo, Kashiwa, Chiba 277-8561, Japan

Correspondence email: fankangli@hotmail.com

Synopsis

We describe the implementation of the high-resolution, neutron, Larmor-diffraction technique using superconducting magnetic Wollaston prisms at the High Flux Isotope Reactor of Oak Ridge National Laboratory. Recent results are discussed.

Abstract

Using superconducting magnetic Wollaston prisms, high-resolution neutron Larmor diffraction has been implemented at the High Flux Isotope Reactor of Oak Ridge National Laboratory (ORNL), Tennessee, USA. This technique allows the inverse relationship between the achievable diffraction resolution and the useable neutron flux to be overcome. Instead of employing physically tilted radio-frequency spin flippers, the method uses magnetic Wollaston prisms which are electromagnetically tuned by changing the field configurations in the device. As implemented, this method can be used to measure lattice spacing changes induced, for example, by thermal expansion or strain with a resolution of $\frac{\Delta d}{d} \sim 10^{-6}$ and the splitting of sharp Bragg peaks with a resolution of $\frac{\Delta d}{d} = 3 \times 10^{-4}$. The resolution for discerning a change in the profile of a Bragg peak is $\frac{\Delta d}{d} < 10^{-5}$. This is a remarkable degree of precision for a neutron diffractometer as compact as the one used in this implementation. Higher precision could be obtained by implementing this technique in an instrument with a larger footprint. The availability of this technique will provide an alternative when standard neutron diffraction methods fail and will greatly benefit the scientific communities that require high-resolution diffraction measurements.

1. Introduction

By measuring the diffraction angle and applying Bragg's law, conventional diffraction techniques using x-rays and neutrons scattering, have shown their importance to determine the atomic and/or magnetic structure of materials. To achieve a lattice-spacing resolution better than $\Delta d/d \sim 10^{-3}$, is extremely challenging for neutrons due to the beam divergence and relatively low neutron flux. However, the neutron, a particle with a magnetic moment of $\mu_n = -1.93\mu_N$ with μ_N being the nuclear magneton, provides us with an alternative way of approaching the problem by using the Larmor precession of its spin in magnetic fields (Bloch, 1946, Mezei, 1972). This method is termed Larmor labeling. The Larmor labeling of neutron spin has been used to encode the change in neutron energy (Mezei, 1972) and trajectory (Rekveldt, 2011). For the energy encoding, dubbed Neutron Spin Echo (NSE) (Mezei, 1972), the small energy change experienced due to quasi-elastic neutron scattering can be encoded into a change in the Larmor phase by using two solenoids whose magnetic fields are parallel to the neutron trajectories before and after scattering. For trajectory encoding, such as Spin Echo Small Angle Neutron Scattering (SESANS) (Rekveldt, 1996, Pynn *et al.*, 2005, Parnell *et al.*, 2015) or Larmor diffraction (Rekveldt *et al.*, 2001, Keller *et al.*, 2002), the change in the neutron trajectory due to the interaction with the sample can also be labelled using the Larmor phase. By measuring the Larmor phase of the overall beam using a polarizing analyzer, structural information about the sample can be recovered. Neutron Larmor diffraction, first introduced by Rekveldt (Rekveldt *et al.*, 2001), generates a Larmor phase that depends only on the scattering vector of the Bragg peak measured. Compared with high resolution X-ray, neutron Larmor diffraction takes

full advantage of the penetrating power of neutrons and allows us to measure samples containing light elements, like oxygen or carbon, as well as magnetic samples in some cases.

The neutron Larmor diffraction concept as introduced by Rekveldt (Rekveldt *et al.*, 2001) involves two rectangular regions of constant magnetic field, located before and after the sample, with their boundaries tilted to be parallel to the diffracting crystal planes in such a way that the total Larmor phase produced by the setup is given by

$$\Phi = \frac{2m\omega_L L}{\pi\hbar} d \qquad (1)$$

, where *m* is the mass of neutron, ω_L is the Larmor frequency given by $\omega_L = \gamma_n B$, *L* is the size of the coil and *d* is the lattice spacing (Rekveldt *et al.*, 2001). Thus, instead of directly measuring the change in the diffraction angle, this method allows the measurement of small changes in the lattice spacing through the change of the neutron Larmor phase Φ, allowing poorly collimated neutron beams to be used and thereby overcoming the limitations imposed by the inverse relationship between the achievable resolution and the useable flux that apply to traditional diffraction measurements.

Even though the use of two rectangular DC electromagnets would be the most straightforward way of implementing Larmor diffraction, the tilt angle is highly constrained since the two electromagnets need to be long enough to reach to a useful resolution range. Therefore, to dateneutron Larmor diffraction has only been implemented using the Neutron Resonance Spin Echo (NRSE) technique (Keller & Keimer, 2015) with thin radio-frequency (RF) neutron resonant flippers rather than DC magnets, as shown in Figure 1 (a). The RF flippers work as external clocks (Gähler *et al.*, 1992), where the first pair times the passage of the incident neutrons and the second measures the scattered neutrons. Due to the energy exchange between the neutron spin and the RF flippers, the neutron polarization vectors will be modulated in the time domain in the zero field regions between the two pairs of RF. Effectively, the modulation in time is equivalent to that of precession in a static field with the same geometry as the zero-field regions defined by the two pairs of RF flippers (so-called zero-field precession). By using a so-called bootstrap mode (Golub & Gähler, 1987), the total Larmor phase given in equation (2) can be increased by a factor of *four* for the NRSE method compared with the DC method with the same dimensions and fields. This technique has been used with great success, for example, to measure the structural and magnetic phase transitions in electron-doped iron pnictides (Lu *et al.*, 2016) and to study the formation of magnetostructural domains in yttrium barium copper oxides, YBCO (Náfrádi *et al.*, 2016).

Recently, we also demonstrated our approach to implementing Larmor diffraction using superconducting magnetic Wollaston prisms (Li *et al.*, 2017, Li *et al.*, 2014, Li, Parnell, Wang, *et al.*, 2016) , as shown in Figure 1 (b) and its principle has been explained and demonstrated (Li & Pynn, 2014, Li *et al.*, 2017). Basically, by using a series of magnetic field boundaries with or without

inclinations, the method provides us with the possibility to tune the effective field boundaries by picking different combinations of the fields. The inclined field boundary is provided by the triangular field regions of the magnetic Wollaston prisms whose boundaries are defined by the Meissner effect of the superconducting YBCO films, as shown in Figure 1 (b). This eliminates the requirement to physically tilt the coils, which means high effective tilt angle can be achieved. Though this approach is a DC method, the total Larmor phase does not take a simple form given in equation (1), owing to the electromagnetic tuning.

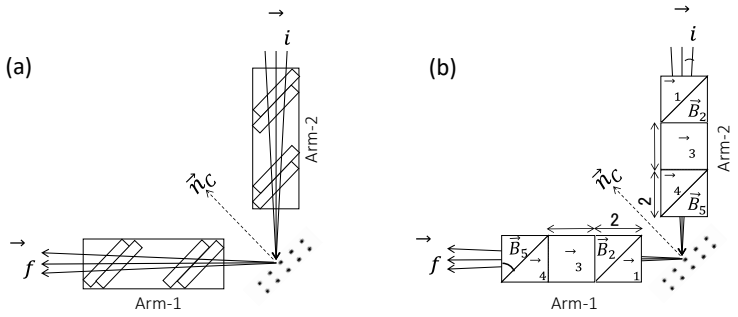

Figure 1 The Larmor diffraction setup using (a) RF spin flippers in bootstrap mode, (b) magnetic Wollaston prisms. For (a), the rectangles with different colours are the RF spin flippers with different field directions. They are enclosed inside a zero magnetic field chamber made of Mu-metal with high magnetic permeability. The tuning is achieved when the field boundaries of the RF flippers are parallel to the crystal plane. For (b), each arm is composed of two superconducting magnetic Wollaston prisms with a rectangular field in between them. The region with the same colour indicates the same magnetic field of both magnitude and direction. All the field boundaries are provided by the Meissner effect of superconducting YBCO films (350nm) coated on 0.5mm sapphire plates (Li *et al.*, 2014). The tuning is achieved when the effective tilt angle of the magnetic field boundary (see equation (25) of (Li & Pynn, 2014)) matches the orientation of the crystal plane. α is the inclination angle of the hypotenuse film inside the Wollaston prism.

2. Larmor diffraction using magnetic Wollaston prisms

The details of tuning the effective tilt angle using magnetic Wollaston prisms have been discussed in refs. (Li *et al.*, 2017, Li & Pynn, 2014) and the experimental tuning results are very close to the calculations. This provides us with confidence to tune the setup on the basis of the calculation results. Once the effective field boundary of the setup has been tuned with respect to the diffracting crystal planes, the accumulated total Larmor phase (Φ) inside the device is only dependent on the d spacing of the crystal and not, to lowest order, on the beam collimation or the crystal mosaic. With the polarization analyzer, only the projection of the polarization vector along the field direction of the analyzer can be picked up, namely $\cos(\Phi)$. Therefore, for a crystal with a distribution of d spacings

whose mean value is $\bar{d}$, the induced Larmor phase variation is $\Phi = \frac{d}{\bar{d}}\bar{\Phi}$ and the neutron polarization measured is the cosine-Fourier transform of the distribution over all the lattice spacings (Keller *et al.*, 2002).

$$P(\Phi) = \int f\left(d, \bar{d}, \sigma\right)\cos(\Phi)\delta(d) \tag{2}$$

Here, in the case of a simple Gaussian distribution of lattice spacings, $f\left(d, \bar{d}, \sigma\right)$ is the normalized distribution function of the lattice spacings, i.e.

$$f\left(d, \bar{d}, \sigma\right) = \frac{2}{\sigma}\sqrt{\frac{ln2}{\pi}}e^{-4ln2(\frac{d-\bar{d}}{\sigma})^2} \tag{3}$$

where σ is the full width half maximum (FWHM) of the distribution. In a more complicated case, as shown in in Figure 2(f), if a Bragg peak is split into two peaks with lattice spacings of d_1 and d_2 and amplitudes a_1 and a_2, f can be written as,

$$f = a_1 f(d, d_1, \sigma_1) + a_2 f(d, d_2, \sigma_2) \text{ with } d_1, d_2 = \bar{d} \mp \frac{\Delta d}{2} \tag{4}$$

where $\bar{d}$ in this case is the average d spacing of all Bragg peaks measured, i.e. $\bar{d}$=$d_1 + d_2$. Its cosine Fourier transform is given as:

$$P(\Phi) = \sqrt{G(a_1, \sigma_1)^2 + G(a_2, \sigma_2)^2 + 2G(a_1, \sigma_1)G(a_2, \sigma_2)\cos(\Phi\frac{\Delta d}{\bar{d}})} \tag{5}$$

where

$$G(a, \sigma) = a\, e^{-\frac{\sigma^2\Phi^2}{16ln2}} \tag{6}$$

The measured trend of polarization P(Φ) is only dependent on the distribution of the d-spacings $\frac{\Delta d}{d}$ rather than on the mean value of the lattice spacing. For this reason, the following discussion will be focused on the distribution of lattice spacings. Figure 2 shows examples of some potential results of Larmor diffraction experiments (top) and the corresponding distributions of the lattice spacings (bottom). Clearly, the measured polarization follows the general expectations for Fourier transformation. For a perfect crystal with a single-valued lattice spacing the amplitude of the Larmor phase oscillations is constant. For a crystal with some broadening in *d* spacing, the measured polarization would damp monotonically towards high neutron Larmor phase. For a Bragg peak splitting, for example d_1 and d_2, each lattice spacing will correspond to an oscillating polarization with a certain frequency when scanning the Larmor phase. Therefore, these two different frequencies will beat with each other, achieving a maximum amplitude of the polarization oscillations when the relative phase difference between the polarization signals for the two Bragg peaks equals $2N\pi$. To be

specific, the beating can be reflected by the oscillation caused by the $\cos\frac{\Delta d}{d}\Phi$ term in equation (5), as shown in Figure 2(c). When the phase between the two different frequencies is $(2N+1)\pi$, they are completely out of phase and a minimum in the polarization will be obtained. For a two-peak splitting in Figure 2(f), the relative splitting of the d-spacings, $\frac{\Delta d}{d}$, is given by $\frac{\pi}{\Phi_{P=0}}$, where $\Phi_{P=0}$ is the Larmor phase at the first minimum of the polarization (Figure 2(c)). For example, if the first minimum of the P(Φ) curve is observed at $\Phi_{P=0} = 1000rad$, the lattice splitting $\frac{\Delta d}{d} = \frac{\pi}{1000}$. So, to some extent, $\frac{\pi}{\Phi_{P=0}}$ gives a good estimate of the achievable resolution for measurements of the difference between two d-spacings that exist in the same sample. For the measurements of the relative change of d-spacing distribution profile (as a function of temperature for example), the achievable resolution will be better ($<10^{-5}$) because we just need to focus on the point with the highest Larmor phase and see how it changes. As also shown in Figure 2(c), the population of the two lattice constants will affect the local amplitude of the oscillation and the broadening of each lattice constant will cause the overall damping of the polarization curve.

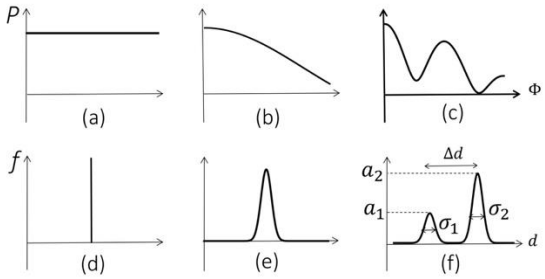

Figure 2 Three typical results (top row) of Larmor diffraction measurements for demonstration and their corresponding distribution of lattice spacings (bottom row).

3. Lattice structural distortion measurements of $CuFeO_2$

The experimental setup for neutron Larmor diffraction with magnetic Wollaston prisms on the HB-1 polarized triple-axis spectrometer (PTAX) at the High-Flux Isotope Reactor (HFIR) of Oak Ridge National Laboratory is shown in Figure 3, with the neutrons traveling from right to the left straight through the sample. To minimize the magnetic stray field in the sample area, the two arms are surrounded by Mu metal plates on the four sides and these plates are connected to the Mu metal chamber for the sample (labeled as ②). The stray field inside the Mu metal chamber can be minimized to <0.1G by using a series of compensation coils. The sample used for this measurement was $CuFeO_2$, which undergoes a first-order structural phase transition induced by the magnetic transition at 11K and a second-order lower symmetry lattice distortion at 14K seen using high-

resolution synchrotron x-ray scattering performed at the 11-ID-C station of Advanced Photon Source, Argonne National Laboratory (Ye et al., 2006). Since lattice expansion measurements on copper have already been demonstrated in ref. (Li *et al.*, 2017), the following part will focus on lattice distortion measurements.

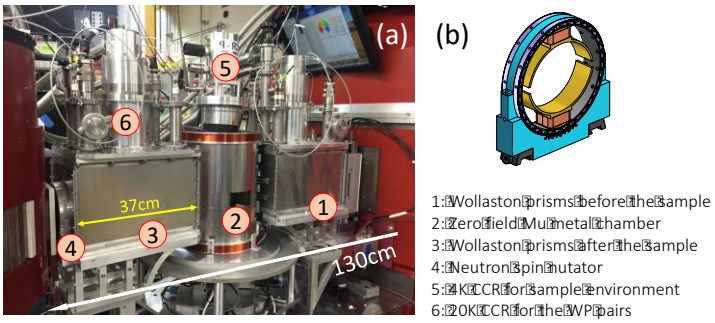

Figure 3 (a) The experimental setup of the Larmor diffraction on HB-1 polarized triple axis spectrometer (PTAX) at HFIR in a transmission geometry for better clarity. Neutrons are traveling from right to left. (b) Drawing of the nutator used in (a), which can create a magnetic field in any direction in the 2-D plane perpendicular to the beam. The space between the exit of the monochromator drum and the entrance of the analyser drum is ~130cm and cannot be changed.

The neutron wavelength used for this measurement was 2.46Å. Heusler (111) was used as monochromator and analyzer. The horizontal collimator sequence was 48'-80'-60'-240' and the contamination from higher-order beams was effectively eliminated using pyrolytic graphite filters.

The measured Bragg peak of $CuFeO_2$ is (012) with $2\theta = 58.75°$, thus the tilt angle needed is $\beta = 60.6°$, (see equations (15) of ref. (Li & Pynn, 2014)) which means the magnetic field ratio needs to be set to $\gamma = \frac{B_4}{B_5} = -4.87$ for the configuration shown in Figure 1 (b). For the NRSE method, the total Larmor phase is obtained by scanning the Larmor frequency ω_L in the RF flippers while keeping the physical field boundaries unchanged and the polarization is then obtained by rocking the distance between the RF flippers (L), as shown in in Figure 1 (a). For our approach with Wollaston prisms, the total Larmor phase is varied by scanning the current inside the device while simultaneously maintaining the effective tilt angle the same (i.e. $\gamma = constant$). To minimize the measuring time, as shown in Figure 4, the Larmor phase is only scanned at 25 current bands, which are the 25 stripes in the plot. For each current (stripe), the polarization ($P = \frac{A}{I}$) is obtained by rocking the current in a small region, where A and I are the amplitude and shim intensity of the fringes shown in the inset figure of Figure 4 (a).

During the experiment, as shown in Figure 4, the fringes as a function of total Larmor phase are obtained for two different temperatures, where (a) is for 6.7K and (b) is for 17K. Clearly, the envelope of the fringes oscillates as a function of Larmor phase at 6.7K while it remains almost flat at 17K, as

reflected by the cosine term in equation (5). The scan of the total Larmor phase was repeated for various temperatures. The polarization efficiencies of all the fringes were extracted for all temperatures and normalized with respect to the polarization efficiency at 17K. Some of the results are shown in Figure 5. Here, results for three different temperatures with the polarization normalized are shown on the left and their corresponding distributions of the lattice constants fitted by equation (4) are given on the right-hand side. At 6.7K, as shown in Figure 5 (a), where the structural distortion is significant, an oscillation can be observed in the polarization. As discussed earlier, this is due to the cosine term in equation (5) and the position of the first minimum gives us a good estimate of the absolute lattice distortion ($\frac{\Delta d}{d} = \frac{\pi}{\Phi_{P=0}}$), For Figure 5 (b), though only five points were obtained, the distribution of lattice constants can be obtained precisely by fitting once the minimum position is known. To obtain a high-resolution measurement of the peak splitting ($\frac{\Delta d}{d}$) in this case, the key is to maximize the achievable Larmor phase, for example by using longer wavelength neutrons or increasing the magnetic field intensity or the size of the device.

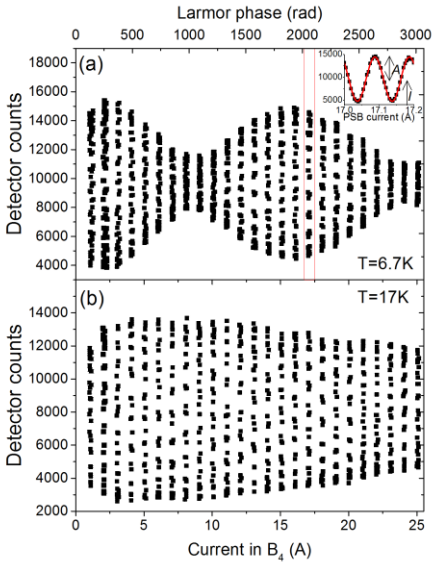

Figure 4 The fringes measured as a function of current B_4 (bottom axis) and the corresponding total Larmor phase is indicated as the top axis: (a) T=6.7*K*, (b) T=17*K*. Each stripe in the plot corresponds to a fringe, shown in the inset plot in (a), which is measured by scanning the current in the device while maintaining the effective tilt angle the same.

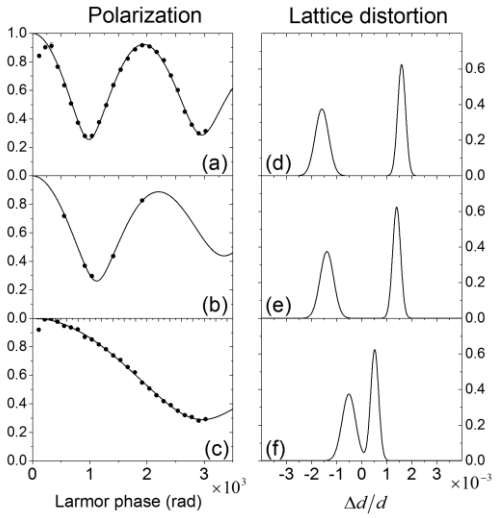

Figure 5 Left: the normalized polarization as a function of Larmor phase for (a) 6.7K, (b) 9.9K and (c) 12K. Right: the distribution of the lattice distortions $\frac{\Delta d}{d}$ with the lattice variation Δd normalized to the mean value *d*, to fit the corresponding polarization on the left. For (b), the polarization efficiency has been measured only at 5 different values of Larmor phase to show the sufficient data fit with them and the populations and the FWHM of the split peaks are kept the same for different temperatures.

The peak splitting $\frac{\Delta d}{d}$ has been plotted as a function of temperature together with the data obtained by X-ray diffraction, which is shown in Figure 6 as the solid circles. Clearly, the values measured by Larmor diffraction well agree with the ones obtained by X-ray diffraction below 12K. The slight difference at 12K is possibly due to the uncertainty of the temperature reading during the two experiments. This can be seen from the difference of the extrapolated critical temperatures for these two measurements, both of which should be 13.5K.

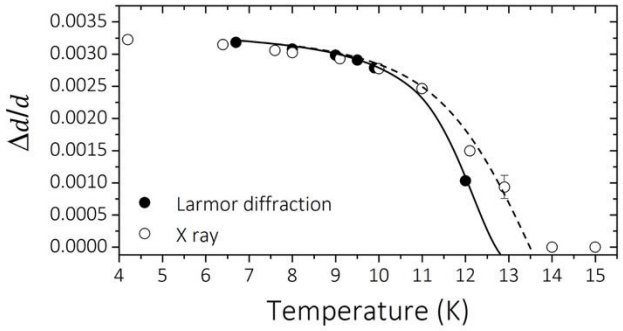

Figure 6 The measured $\frac{\Delta d}{d}$ as a function of temperature for $CuFeO_2$. The solid and hollow circles are the values obtained by Larmor diffraction and X-ray diffraction correspondingly. Due to the limited number of data points, the lines are a guide to the eye to show the critical temperature discrepancy

between these two methods. The error bars for the Larmor diffraction measurements are smaller than the size of the points.

4. Discussion

4.1. Collimation of the host triple axis spectrometer

For this technique, the host triple axis spectrometer (TAX) needs to be positioned to observe the Bragg peak of interest. Splitting of Bragg peaks due to structural distortion can be extremely hard to be measure using a 2θ scan of a TAX due to the beam divergence. By encoding the diffracted neutron trajectories into different Larmor phase, these split Bragg peaks are labelled with different Larmor phases which causes the beating of the measured polarization as we observed. A prerequisite condition of this technique is to capture all the diffracted neutrons from all the lattice distortions. For example, if the lattice distortion is large enough that some of the diffracted neutrons fall out of the detector or are cut off by the collimator after the sample, the setup is not performing a complete Fourier transform and we could not get the correct answer. Therefore, Larmor diffraction is similar to other neutron Larmor labelling techniques (Parnell *et al.*, 2015, Li, Parnell, Bai, *et al.*, 2016), in that all the scattered or diffracted neutrons need to be detected. Based on Bragg's law $\lambda = 2d\sin\theta$, to measure a lattice distortion of $\frac{\Delta d}{d}$ for a lattice spacing of *d*, the minimum collimation after the analyzer is $\Delta\theta = \theta\tan(\theta)\frac{\Delta d}{d}$. For example, for $2\theta = 58.75°$ and $\frac{\Delta d}{d} = 3\times10^{-3}$, the minimum collimation allowed for the outgoing neutrons is ~0.05°, which is much smaller than the typical collimator used on TAX. For the incoming neutrons, the divergence of the neutron beam will cause Larmor phase aberration for the measured polarization and this will give an intrinsic resolution of the setup, as discussed in ref. (Rekveldt *et al.*, 2014). So the incoming neutron beam needs to be well collimated.

4.2. Optimization of the achievable Larmor phase

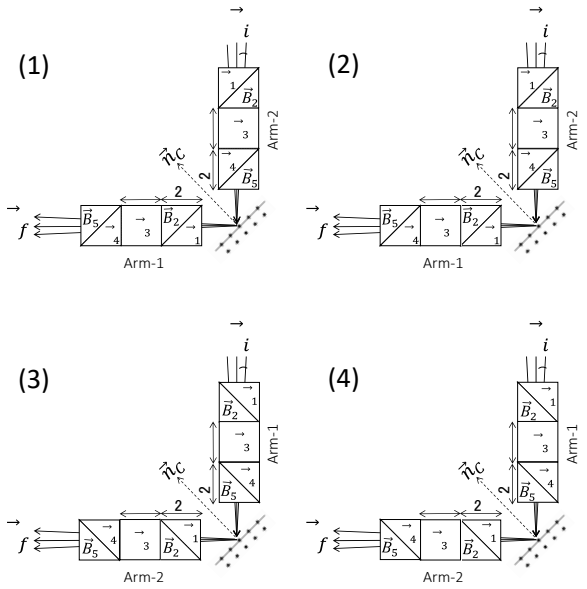

Figure 7 The schematics of the possible Larmor diffraction setups using the magnetic Wollaston prisms. Regions with the same colour have the same magnetic field intensity and direction. Compared with the configurations on the top (1, 2), these two arms are swapped in the bottom configurations (3, 4).

Figure 1 (b) shows only one of the configurations to operate the device for Larmor diffraction, to be specific, $B_1 = B_5$ and $B_2 = B_3 = B_4$. Based on ref. (Li & Pynn, 2014), any of configurations that can keep $B_1 - B_2 + B_4 - B_5 = 0$ can be employed. Therefore, it could also be connected such that $B_2 = B_4$ and $B_1 = B_3 = B_5$. Since the sense of the hypotenuse films for the Wollaston prisms in these two arms are opposite to each other, these two arms can also be swapped with respect to the sample position. In principle, the rectangular field in between the two Wollaston prisms is not related to the field inside the Wollaston prisms but to reduce the number of power supplies required and simplify the operations, it is connected in series to the other field regions. The possible Larmor diffraction setups using the Wollaston prisms have been summarized in Figure 7.

Table 1 The chart for the possible field configurations in Figure 7. ARM-1 upstream means the setup would be the same as the configurations on the bottom of Figure 7 while in ARM-2 upstream configuration, the two arms are swapped. γ_n is the gyromagnetic ratio of the neutron, m is the neutron mass, h is Planck's constant and λ is the neutron wavelength.

	Configuration	$\boldsymbol{\gamma = B_4/B_5}$	Total Larmor phase $\boldsymbol{\Phi}(\times\frac{\gamma_n m\lambda}{h})$
1	$B_1 = B_5$ $B_2 = B_3 = B_4$	$\frac{S + 2D(1+\tan\beta)}{(S+2D)(1-\tan\beta)}$	$2[(S+2D)\gamma + 2D]B_5$

2	$B_2 = B_4$ $B_1 = B_3 = B_5$	$\frac{(S+2D)(1+\tan\beta)}{S+2D(1-\tan\beta)}$	$2[(S+2D)+2D\gamma]B_5$
3	$B_1 = B_5$ $B_2 = B_3 = B_4$	$\frac{S+2D(1-\tan\beta)}{(S+2D)(1+\tan\beta)}$	$2[(S+2D)\gamma+2D]B_5$
4	$B_2 = B_4$ $B_1 = B_3 = B_5$	$\frac{(S+2D)(1-\tan\beta)}{S+2D(1+\tan\beta)}$	$2[(S+2D)+2D\gamma]B_5$

In Table 1, we list the configurations shown in Figure 7, including the calculations of the ratio of $\gamma = B_4/B_5$ for a given tilt angle β and the corresponding Larmor phase Φ. As discussed earlier, the highest Larmor phase will determine the resolution of the setup. For each configuration, the highest achievable Larmor phase for each effective tilt angle has been calculated and plotted in Figure 8. In the calculations, we have used parameters for our device, namely a maximum current of 50A with a magnetic field of 35G/A, a footprint of 37cm for each arm and a neutron wavelength of 2.46 Å. Clearly, the highest Larmor phase of this technique is coupled with the effective tilt angles. Specifically, the overall Larmor phase for high effective tilt angle is lower. For example, to achieve a tilt angle beyond 45° using the setup shown in Figure 1 (b), the field directions of B_1 and B_5 have to be the opposite to B_2, B_3 and B_4, which means the Larmor phase generated in B_1 and B_5 will be subtracted from that accumulated in B_2, B_3 and B_4. While for an effective tilt angle lower than 45°, B_1 and B_5 need to be the same direction as B_2, B_3 and B_4, which will add additional Larmor phase. Equivalently, the effective tilt will lead to an effective size of the magnet, given as the coefficient of the B_5 in Table 1. This is different from that of the NRSE technique, where the Larmor phase is a constant for all the tilt angles, since the length of the flight path does not change when changing the tilt angles, as shown in Figure 1(a). On the other hand, by introducing effective tilt using Wollaston prisms, the polarization and transmission efficiency of the setup is not affected when changing the effective tilt angle since no physical movement of the coils is required. From the calculations, we can see that configurations 1 and 4 are similar and always have the highest Larmor phase. With a maximum total Larmor phase of 12000 rad, to observe at least one minimum in Figure 2(c) for a measurement of Bragg peak splitting, this means a resolution of $\frac{\Delta d}{d} \sim \frac{\pi}{\Phi_{P=0}} \sim 3 \times 10^{-4}$. However, the resolution may be higher ($< 10^{-5}$) for discerning a change in the profile of a Bragg peak as a function of an external parameter such as temperature. Currently, the achievable resolution is constrained by the available space on the beamline, as shown in Figure 3 and the fact that the largest useable neutron wavelength is limited to 2.46Å since the host TAX beamline is on a thermal neutron moderator.

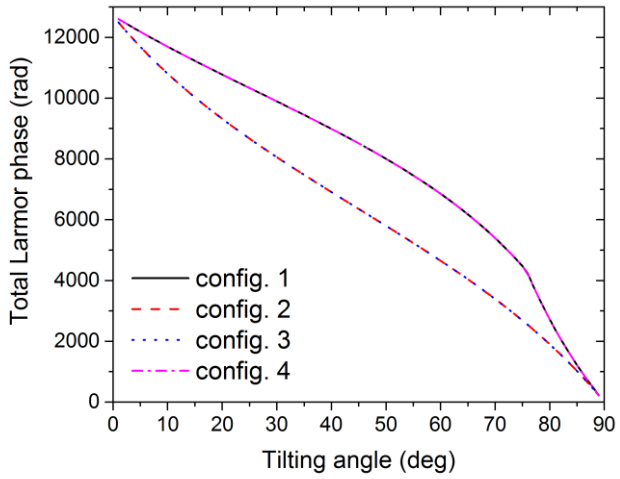

Figure 8 The map of the maximum accessible total Larmor phase for each configuration listed in Table 1. The maximum current allowed inside the device is 50A and the magnetic field achieved is 35G/A. The dimension used, as shown in Figure 1, are: *S*=*2D*=10.5cm, and the wavelength used is 2.46Å.

5. Conclusion

We have successfully implemented high-resolution neutron Larmor diffraction using superconducting magnetic Wollaston prisms on a polarized-neutron triple-axis spectrometer located at the HFIR at ORNL. Using this technique, we can measure the splitting of a sharp Bragg peak with a resolution of $\frac{\Delta d}{d} = 3 \times 10^{-4}$ and the resolution for discerning a change in the profile of a Bragg peak can be $\frac{\Delta d}{d} < 10^{-5}$. For lattice changes induced by thermal expansion or strain, a resolution better than what has been presented in ref. (Li *et al.*, 2017) can be achieved. After 3-4 hours of warming up the main power supply and employing another precise and stable power supply in parallel, a resolution of $\frac{\Delta d}{d} \sim 10^{-6}$ has been achieved to measure the thermal expansion. This is a remarkable degree of precision for a neutron diffraction setup as compact as the one used in this implementation. Although an X-ray diffractometer can be configured to achieve a similar resolution, the wavelength spread needs to be minimized using a double-bounce monochromator and the method is limited to some specific samples. The achievable resolution of this setup is equivalent to that of the TRISP instrument at the FRM-II reactor in Germany (Keller & Keimer, 2015).

YBCO is a type-II superconductor, which means magnetic flux can penetrate when the YBCO film experiences a large enough perpendicular magnetic field (Brandt, 1996). To achieve even higher field thus resolution, thicker YBCO film is required and its development is still under investigation.

The purpose of involving two Wollaston prisms in each arm is to introduce a combination of inclined and non-inclined magnetic field boundaries such that the effective field boundaries can be varied by picking the right combination of them. The current inclination angle (α in Figure 1) is 45°. For a given space available, reducing this angle can shrink the size of the Wollaston prism along the beam direction and thus increase the size of the rectangular field region in between, which can be also be used to generate a larger Larmor phase without increasing the size of the device.

6. Acknowledgement

This research is sponsored by the Laboratory Directed Research and Development Program of Oak Ridge National Laboratory, managed by UT-Battelle, LLC, for the U. S. Department of Energy. This research used resources at the High Flux Isotope Reactor, a DOE Office of Science User Facility operated by the Oak Ridge National Laboratory. We would like to acknowledge the team members of the HFIR, Gerald Brent Taylor, Harish Agrawal, Ron G Maples, John Ray Stout, Ron Conaway, John William Carruth, Stephen Kulan and Gary A. Taufer, for their help with the experiments. We are also indebted to Thomas Keller for useful discussions and support.

7. Reference

Bloch, F. (1946). *Phys. Rev.* **70**, 460-474.

Brandt, E. H. (1996). *Phys. Rev. B* **54**, 4246-4264.

Gähler, R., Golub, R. & Keller, T. (1992). *Physica B* **180–181, Part 2**, 899-902.

Golub, R. & Gähler, R. (1987). *Phys. Lett. A* **123**, 43-48.

Keller, T. & Keimer, B. (2015). *Journal of large-scale research facilities* **1**, A37.

Keller, T., Rekveldt, M. T. & Habicht, K. (2002). *Appl. Phys. A* **74**, s127-s129.

Li, F., Feng, H., Thaler, A. N., Parnell, S. R., Hamilton, W. A., Crow, L., Yang, W., Jones, A. B., Bai, H., Matsuda, M., Baxter, D. V., Keller, T., Fernandez-Baca, J. A. & Pynn, R. (2017). *Scientific Reports* **7**, 865.

Li, F., Parnell, S. R., Bai, H., Yang, W., Hamilton, W. A., Maranville, B. B., Ashkar, R., Baxter, D. V., Cremer, J. T. & Pynn, R. (2016). *J. Appl. Crystallogr.* **49**, 55-63.

Li, F., Parnell, S. R., Hamilton, W. A., Maranville, B. B., Wang, T., Semerad, R., Baxter, D. V., Cremer, J. T. & Pynn, R. (2014). *Rev. Sci. Instrum.* **85**, 053303.

Li, F., Parnell, S. R., Wang, T., Baxter, D. V. & Pynn, R. (2016). *Journal of Physics: Conference Series* **711**, 012015.

Li, F. & Pynn, R. (2014). *J. Appl. Crystallogr.* **47**, 1849-1854.

Lu, X., Tseng, K.-F., Keller, T., Zhang, W., Hu, D., Song, Y., Man, H., Park, J. T., Luo, H., Li, S., Nevidomskyy, A. H. & Dai, P. (2016). *Phys. Rev. B* **93**, 134519.

Mezei, F. (1972). *Z. Physik* **255**, 146-160.

Náfrádi, B., Keller, T., Hardy, F., Meingast, C., Erb, A. & Keimer, B. (2016). *Phys. Rev. Lett.* **116**, 047001.

Parnell, S. R., Washington, A. L., Li, K., Yan, H., Stonaha, P., Li, F., Wang, T., Walsh, A., Chen, W. C., Parnell, A. J., Fairclough, J. P. A., Baxter, D. V., Snow, W. M. & Pynn, R. (2015). *Rev. Sci. Instrum.* **86**, 023902.

Pynn, R., Fitzsimmons, M. R., Fritzsche, H., Gierlings, M., Major, J. & Jason, A. (2005). *Rev. Sci. Instrum.* **76**, 053902.

Rekveldt, M. T. (1996). *Nucl. Instrum. Methods Phys. Res., Sect. B* **114**, 366-370.

Rekveldt, M. T., Keller, T. & Golub, R. (2001). *EPL (Europhysics Letters)* **54**, 342.

Rekveldt, M. T., Plomp, J. & van Well, A. A. (2014). *J. Appl. Crystallogr.* **47**, 436-442.

Rekveldt, T. (2011). *Physica B* **406**, 2324-2332.

Ye, F., Ren, Y., Huang, Q., Fernandez-Baca, J. A., Dai, P., Lynn, J. W. & Kimura, T. (2006). *Phys. Rev. B* **73**, 220404.